Marine and Petroleum Geology 68 (2015) 776–788

Contents lists available at ScienceDirect

Marine and Petroleum Geology

journal homepage: www.elsevier.com/locate/marpetgeo

Research paper

Long-term acoustic monitoring at North Sea well site 22/4b

Sean M. Wiggins[a,*], Ira Leifer[b,c], Peter Linke[d], John A. Hildebrand[a]

[a] Scripps Institution of Oceanography, 9500 Gilman Drive, La Jolla, CA 92093-0205, USA
[b] Bubbleology Research International, Solvang, CA 93463-2613, USA
[c] Marine Science Institute, University of California, Santa Barbara, CA 93106-1080, USA
[d] Helmholtz Centre for Ocean Research Kiel (GEOMAR), Wischhofstr. 1-3, 24148 Kiel, Germany

ARTICLE INFO

Article history:
Received 20 December 2013
Received in revised form 30 January 2015
Accepted 10 February 2015
Available online 26 February 2015

Keywords:
Marine seep
Passive acoustic monitoring
Methane
Bubble plume

ABSTRACT

Marine seeps produce underwater sounds as a result of bubble formation and fragmentation upon emission from the seabed. The frequency content and sound levels of these emissions are related to bubble size distribution and emission flux, providing important information on methane release from the seafloor. Long-term passive acoustic monitoring was used to continuously record seep sounds over a 7-month period within the blowout crater at the abandoned well site, 22/4b, in the central North Sea. Also recorded were water column fluid velocities and near-seafloor water conductivity, temperature, and pressure. Acoustic signatures were primarily from ~1 to 10 kHz. Key features were relatively broad spectral peaks at about 1.0, 1.5, 2.2, 3.1, 3.6 and 5.1 kHz. Temporal variations in spectral levels were apparently associated with tides.

The recordings also documented a series of major episodic events including a large and persistent increase (~10 dB) in overall sound levels and spectral broadening on 8 December 2011. The acoustic temporal pattern of this event was consistent with other recorded large transient events in the literature, and the major event was correlated with dramatic changes in other measurements, including increased water column fluid velocities, increased pressure and decreased salinity, indicating real changes in emission flux. Observed seabed morphology changes reported elsewhere in this special issue, also likely were related to this event. These data demonstrate the dynamic nature of marine seepage systems, show the value of monitoring systems, and provide direct supporting evidence for a violent formation mechanism of many widespread seep-associated seabed features like pockmarks.

1. Introduction

Despite its importance as a potent greenhouse gas (IPCC, 2007), methane (CH_4) has large emission flux uncertainties from well-known sources, like fossil fuel industrial emissions (Peischl et al., 2013), and even larger uncertainties from many sources that are potentially important, but poorly characterized including marine geology and hydrates (Kvenvolden and Rogers, 2005), and submerged Arctic permafrost (Shakhova et al., 2013). These uncertainties arise in part due to the paucity of measurements, highlighting the need for new technologies to measure emission fluxes, particularly approaches that can remotely sense and quantify emissions and have a monitoring capability spanning a wide range of time periods, characterizing variability on sub-second to annual and longer timescales.

Various approaches have been developed to measure bubble fluxes from marine seeps including active acoustics (Schneider von Deimling et al., 2010), video (Mastepanov et al., 2008), direct flux measurements based on flow (Leifer et al., 2004), gas capture (Washburn et al., 2005; Leifer, 2015), and passive acoustics (Leifer and Tang, 2007). Benefits of passive acoustic monitoring (PAM) are low cost, wide bandwidth (i.e., sensitive over large ranges of bubble size and flow rates), manageable data rates, and remote monitoring distant seepage emissions whose precise location is uncertain or variable. Significant analytic and technical capabilities have been developed for PAM of cetaceans (e.g., Wiggins, 2003; Zimmer, 2011) and other marine sounds such as ships (e.g., McDonald et al., 2006; McKenna et al., 2012) which can be applied to marine seeps.

Several PAM features are highly advantageous for application to long-term marine seep monitoring. Specifically, seepage is known to exhibit spatial variability, with vents activating and de-activating (Boles et al., 2001; Leifer et al., 2004). Thus, a fixed monitoring system, like direct flux-measurement that covers a fixed footprint or video, would characterize spatial emission variability as purely

* Corresponding author. Tel./fax: +1 858 822 2744.
E-mail address: swiggins@ucsd.edu (S.M. Wiggins).

http://dx.doi.org/10.1016/j.marpetgeo.2015.02.011

temporal. Although passive acoustic recorders often are fixed spatially, acoustic energy is received from various ranges allowing triangulating with multiple sensors to localize and discriminate between sources (e.g., Wiggins et al., 2013).

Seep bubble PAM primarily records the bubble formation sound, which occurs due to pinching off for low emission gas flows, and is mechanistically and thus acoustically similar to formation from a capillary tube (Vazquez et al., 2005; Leifer and Tang, 2007). Low flows produce plumes with narrow bubble size distributions that are well described as Gaussian and are termed minor seeps (Leifer and Boles, 2005a). High flow plumes produce bubbles by fragmentation within a turbulent jet and bubble size distributions that are well characterized by a power law (Leifer and Boles, 2005a; Leifer and Culling, 2010), as their sound is formed by overlapping acoustic emissions of bubbles of varying sizes and hence varying frequencies as well as scattering and acoustic coupling that shifts the formation frequencies (Vazquez et al., 2005; Leifer and Tang, 2007). Finally, plumes of intermediate flow or unusual orifice shapes can have bubble plume size distributions that contain characteristics of both minor and major plumes (Leifer and Culling, 2010). As a result, intermediate plumes are hypothesized to share acoustic characteristics of both minor and major plumes.

For minor plumes, as each bubble forms it generates a sound whose frequency, f, is proportional to the bubble equivalent spherical radius, r, (and pressure, P_A) by (Minnaert, 1933):

$$f = \frac{1}{2\pi r}\sqrt{\frac{3\gamma P_A}{\rho}} \quad (1)$$

where, ρ is seawater density, and γ is the heat capacity ratio, ~1.32, for methane. Based on (1), each recorded bubble frequency provides a volume via its radius that can be counted and summed with other bubbles over time to estimate flux for that plume. Modification to f occurs where bubbles escape within a few bubble radii of each other, allowing acoustic coupling between the two bubbles, which shifts f (Leifer and Tang, 2007). Furthermore, the acoustic source only persists for a few cycles, damping very rapidly thereafter (Leifer and Tang, 2007).

An alternative approach to estimating seep flux has been proposed by Leighton and White (2012) with which they demonstrated using the field and lab data of Leifer and Culling (2010) for minor and major seeps offshore of Santa Barbara, California at the Coal Oil Point seep field. Their approach uses the recorded far-field sound pressure spectrum in a matrix inversion to estimate the bubble generation rate over a range of bubble radii. One of the key parameters to estimating bubble size distributions with this method is to know the distance of the source vent to the hydrophone because the source spectrum magnitude is related to the bubble generation rate magnitude and ultimately the vent flux. Although source-receiver range is straightforward in a laboratory setting and has been used to verify this model (Chen et al., 2012), seabed seepage emissions often arise from numerous vent locations that often are not precisely known and can vary spatially over time. Examples of such sites have been described (Quigley et al., 1999; Leifer and Boles, 2005a; Greinert, 2008; Leifer et al., 2010). Even for more singular emission sites, such as in Sauter et al. (2006), the vent locations may vary spatially over time as the primary migration pathways are activated and de-activated. The solution, therefore, involves an array of appropriately positioned hydrophones to localize source emissions and to provide source spectrum level estimates used in the inversion analysis to derive emission fluxes.

The 22/4b bubble megaplume (emissions $> 10^6$ L d^{-1}) is located in the central North Sea (Fig. 1) and is a persistent seepage site since its 1990 blowout (Rehder et al., 1998; Schneider von Deimling et al., 2007, 2015; Leifer and Judd, 2015). The 22/4b plume is comprised of bubbles that originate from hundreds of individual vents largely constrained to the ~20 m diameter bottom of an approximately conical crater at 120 m depth, which has its ~60 m diameter rim at 96 m depth (Fig. 2) (Leifer, 2015). A few of these plumes were of the intense major class and were the primary contributor to the overall seabed flux, estimated at 90 L s^{-1}, with significant contribution to overall flux from intermediate flux plumes (Leifer, 2015).

For this study, the 22/4b site provided a test-bed for long-term acoustic observations of a megaplume seep area. Passive observations were made from a protected (viz. trawling) ledge deep in the crater, that was nearby but somewhat separated from bubble plume emissions (Fig. 2). Herein, we present seven months of passive acoustic observations of site 22/4b spanning 2011–2012, which documented significant temporal variability of both cyclical and transient natures. During this period, tidally-related acoustic trends were observed, with several bubble plume emission modes identified.

The most significant temporal change was observed December 2011 when a series of large transient events occurred. The transient events were accompanied by several short acoustic cessation periods followed by a persistent increase in acoustic energy, a change in instrumentation depth, as well as far stronger plume-driven fluid flows. Upon instrumentation retrieval in 2012, a new gash was observed in the nearby crater wall from which escaped a new, very intense major bubble plume (Fig. 3). All these observations are consistent with a strong ejective or eruptive event. Eruptive events are proposed to be important to the formation of common seep related seabed features, pockmarks (Judd and Hovland, 2009). The acoustic monitoring data presented herein provide the first detailed look at this violent seepage process, providing insights into understanding pockmark formation processes and their relationship to seabed CH_4 emission.

2. Methods

2.1. Long-term monitoring of 22/4b

Seepage is known to vary on a range of timescales from subsecond (Leifer et al., 2004) to decadal (Bradley et al., 2010). To assess seep activity and variability at the 22/4b site, long-term monitoring was employed from an autonomous seafloor-mounted platform, the Benthic Lander (Linke, 2011 – Fig. 4). The lander was equipped with a passive broad-band hydrophone to record a wide range of sounds continuously with high temporal resolution; an acoustic Doppler current profiler (ADCP) to record vertical and horizontal ocean currents as a function of depth; and a conductivity-temperature-depth (CTD) sensor to record seabed water salinity, temperature, and pressure (proxy for depth and tidal height). Two landers were deployed sequentially at the same location from 7 June 2011 to 9 September 2011 and from 9 September 2011 to 19 April 2012 at 57° 55.401′N, 01° 37.938′E by lowering on a cable from the Dutch survey vessel *S/V Noordhoek Pathfinder* and then guided by a Remotely Operated Vehicle (ROV) to a small ledge inside the crater at ~112 m depth (Fig. 2). During deployment of both landers, ROV video showed an apparent lack of seepage in the lander's immediate vicinity, although several small plumes were noted a few meters distant.

2.2. Passive acoustic monitoring

To monitor underwater sounds over long periods near the bottom of the 22/4b site crater, a High-frequency Acoustic Recording Package (HARP) data logger, battery, and hydrophone were attached to a Benthic Lander. The two sequential deployments provided two continuous acoustic recordings for over three and four months, respectively. The HARP instrument is described in Wiggins

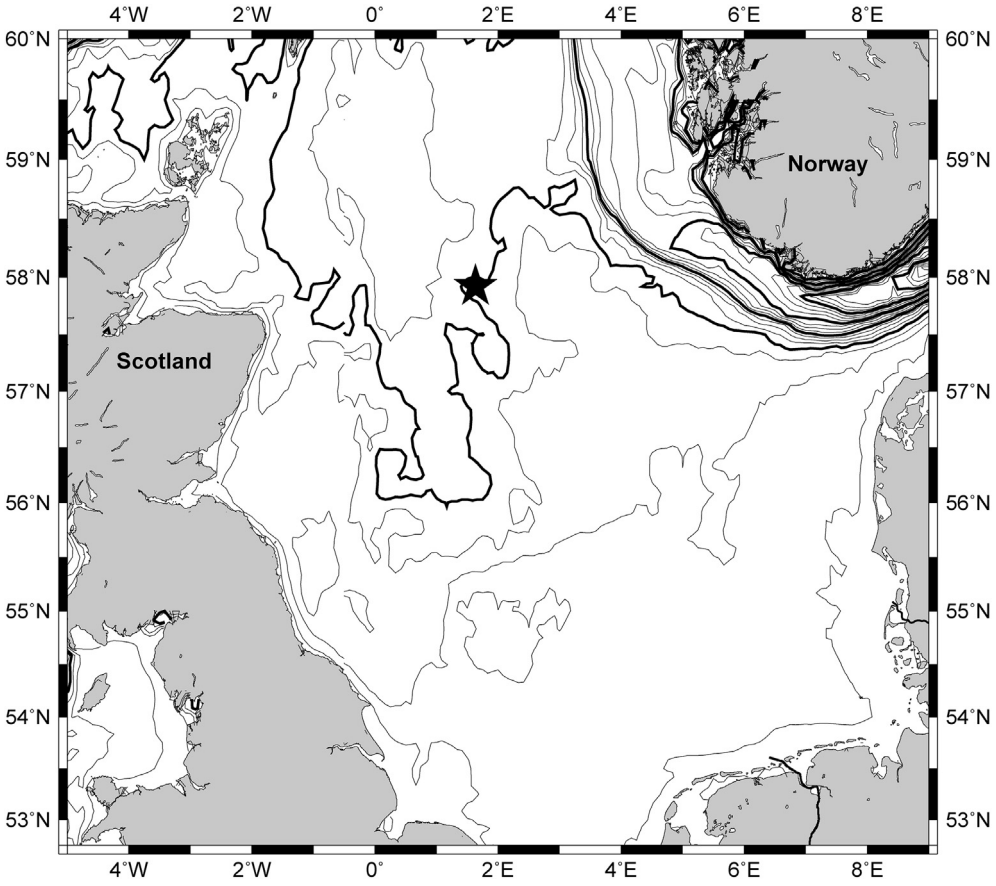

Figure 1. Bathymetric map of the North Sea with Benthic Lander and HARP deployment site at abandon well site 22/4b indicated by star between Scotland and Norway at 57° 55.401′N, 01° 37.938′E, ~112 m deep. Thin contours are at 25 m intervals, thick contours are at 100 m intervals, and land masses are light gray. Bathymetry data are from European Marine Observation and Data Network.

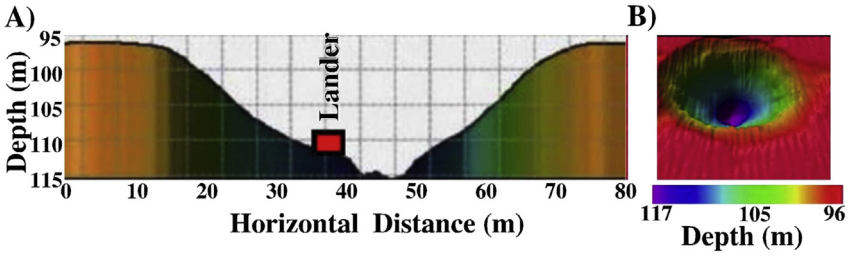

Figure 2. A) Cross-section depth profile through 22/4 b crater including Lander/HARP deployment site on a ledge ~10 m horizontal distance from deepest (119.5 m) portion of crater, and B) overall 22/4b crater bathymetry.

and Hildebrand (2007). In brief, HARPs record broad-band underwater sound at 200,000 samples s^{-1} with an effective bandwidth from 10 Hz to 100 kHz and ~10 months of continuous data storage onto an array of large capacity 2.5″ laptop-type computer hard disk drives. Each HARP is laboratory calibrated to provide a quantitative record of the received sound field. Representative data loggers and hydrophones also have been calibrated at the U.S. Navy's TRANDEC facility in San Diego, California to verify the laboratory calibrations. For both deployments, the hydrophone was mounted 0.65 m above the seafloor, horizontally within the Benthic Lander frame above the syntactic flotation (Fig. 4).

2.3. Acoustic data analysis

Two acoustic datasets were recorded from 13 June to 9 September 2011 and from 9 September 2011 to 8 January 2012. Upon recovery, HARP data disks were removed from the instrument and processed for quality evaluation, archiving, and analysis. HARP data were recorded in a compressed format sequentially to 16 individual hard disk drives. An exact copy of the data from each HARP hard disk was made into a single large (120 GB or 320 GB) file disk image. Then, data from each disk image were uncompressed and saved into many smaller (~1 GB) XWAV files. XWAVs are an enhanced version of the standard loss-less audio format, wav, and include additional meta-data such as data timing, location, and instrument and experiment identification. In addition to full band (100 kHz) data, decimated XWAVs were generated using a factor of 8 and 100 resulting in datasets with 12.5 kHz and 1 kHz bandwidth, respectively. These decimated datasets allow for less computationally intensive, and therefore more efficient, data analysis for low-to mid-frequency sounds.

Long-term spectral averages (LTSAs) were computed for the full band and decimated datasets and are an efficient means of evaluating long periods of acoustic data (see Wiggins and Hildebrand,

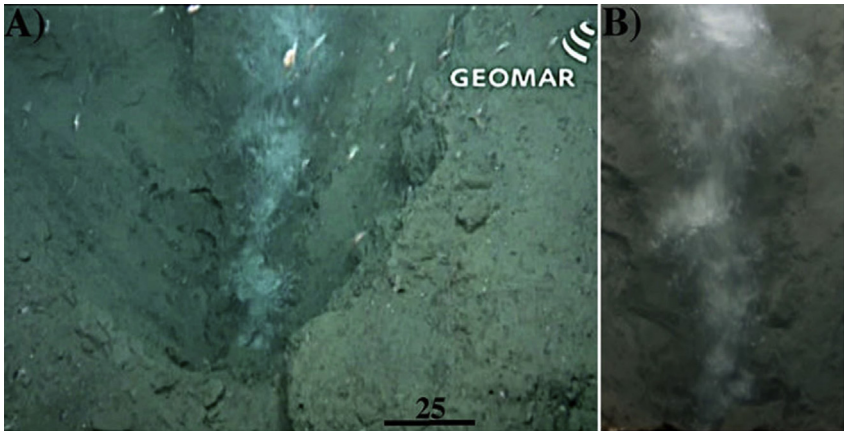

Figure 3. Images of new rift and very strong bubble plume in the 22/4b crater wall. Some large bubbles from small seepage outside the rift are visible in A), scale bar units are cm. B) closer view of the new bubble plume. Collected by ROV KIEL 6000 with the *R/V Celtic Explorer* on 1 August 2012.

2007). LTSAs are spectrograms with each time slice typically covering a window of many seconds (5 s for analysis here) that consist of an average of many (1000 for the full band and 125 for the decimated data), non-overlapping, fast Fourier transforms (FFTs). FFTs were calculated using Welch's method (Welch, 1967) with Hanning windows. LTSA spectral averaging allows hours-long to days-long spectrograms to be displayed and analyzed. In addition, LTSAs provide a graphical means to access the original data easily as waveforms, spectra, and standard spectrograms for further fine-scale investigation of sounds of interest. The sets of average spectra comprising the LTSA time slices also can be used as a basis for additional analysis such as calculating and comparing average spectra over various periods from minutes to months.

Average sound pressure spectral levels were calculated for various time intervals, for example, 15-min, 1-h, one-day, one-month, and for a full deployment from the LTSA, but differences were small, so spectral level mean-differenced anomalies were calculated. To provide a single measure of acoustic power anomaly for each interval-average, the spectral level anomalies were averaged across a band of frequency bins of interest, such as 1–3 kHz, which are known to be important for bubble acoustic emissions (Leifer and Tang, 2007). The acoustic anomalies for the different intervals were plotted versus time, superimposed over the LTSAs to evaluate changes in acoustic emission energy. The acoustic anomaly, A_j, for each time slice j was calculated using Equation (2), where S_{ij} is the interval-average sound pressure spectral level matrix, $\bar{S}_i = 1/N \sum_{j=1}^{N} S_{ij}$ is the average spectra over the deployment of N time slices, and M is the number of frequency bins, i, across the band of interest, f_1 to f_2.

$$A_j = \frac{1}{M} \sum_{i=f_1}^{f_2} \left(S_{ij} - \bar{S}_i \right) \tag{2}$$

LTSAs allow efficient identification of many sounds that are of short duration (<1 ms to >10 s) and repetitive, such as biological sounds from whales and dolphins (e.g., Oleson et al., 2007; Soldevilla et al., 2008; Baumann-Pickering et al., 2010) and anthropogenic sounds, such as from ship echosounders. Alternatively, the acoustic signature from ship propeller bubble cavitation is notably different and appears in LTSAs with much longer durations (minutes to hours) and at low frequencies, often with varying intensity interference patterns (e.g., McKenna et al., 2012). Many natural, abiotic sounds have patterns that occur on even longer timescales (hours to days or longer) such as storms (i.e., rain, wind, breaking waves), underwater currents, and seep bubble emissions. To help separate various natural abiotic sounds, additional ancillary information from other sensors can be used for correlation analysis with the acoustic recordings. For example, wind and rain data from above the sea surface can be compared to the mid-frequency band (~1000–20,000 Hz), and subsurface pressure and currents from ADCP data can be compared with low frequency (<1000 Hz) sound.

Figure 4. Photograph of Benthic Lander with HARP prior to deployment. Hydrophone is mounted horizontally above right-hand side orange tube toward the center of the lander, ADCP is yellow and pointing upward, and CTD is mounted horizontally to the frame (photograph by Peter Linke – GEOMAR). (For interpretation of the references to color in this figure legend, the reader is referred to the web version of this article.)

2.4. ADCP monitoring

A Teledyne/RD Instruments Workhorse ADCP (http://www.rdinstruments.com, 01/15/2015) was employed on both landers providing water column fluid velocities from 7 June 2011 to 19 April 2012. The ADCP transmitted 300 kHz, 2-ms pulses every 18 s from its four beams to measure precisely the Doppler frequency shift from pulse echoes off moving particles (passive flow tracers) in the water from near the seafloor to near the sea surface. Water column current speed and direction are estimated from the Doppler shift over a range of depths. Typically, strong upwards vertical fluid velocities, V_{up}, are not expected for a site over 200 km offshore with no positive seabed bathymetric relief to drive V_{up},

thus, the strong upwelling flows measured at 22/4b (Nauw et al., 2015) clearly relate to bubble-plume processes, specifically the upwelling flow (Leifer et al., 2009). These flow measurements are of fluid motions in the momentum plume surrounding the main plume (Asaeda and Imberger, 1993), because ADCPs cannot measure directly in bubble plumes.

One key ADCP assumption is that the flow field is uniform across the area of the beams (SonTek, 1990). Thus, velocities farther from the ADCP (i.e., shallower) are averaged over a larger volume. The uniform assumption causes erratic velocities when bubbles are present in the volume as they are not passive flow tracers (i.e., scatterers), but have a size-dependent, rise velocity distinct from the fluid's, and their velocity tends to be highly heterogeneous (i.e., dissimilar in the four beams). Moreover, bubbles are strong sonar targets due to their large water-gas impedance difference, compared to the typical small but far more numerous marine particles, thus the bubble impact on data quality is highly magnified. As a result, the ADCP derives erroneous velocities or no velocity at all from bubble-contaminated data or if bubble scattering prevents a return signal. Based on an assumption of fluid flow continuity, good velocity measurements close in time and space were required to be similar or correlated. Thus, bubble-contaminated data were identified by using a five point square median filter in time and range where velocity vectors more than one standard deviation from the mean were removed from the dataset as outliers.

Given that the momentum plume upwelling flow decreases with distance from the bubble plume (Milgram, 1983), ADCP volumetric averaging implies that derived velocities are lower than the peak velocities in the measurement volume, with greater averaging nearer the sea surface where beam spread is larger. To some extent, spreading of the momentum plume (Wüest et al., 1992) will compensate this effect.

In general, the upwelling flow should be strongest right above bubble blanked zones, which is where the ADCP shifts from pinging at bubbles to pinging at the surrounding momentum plume; furthermore, because the ADCP beams are pointed up towards the sea surface, a plume must rise at an angle with horizontal currents, for example from tides, inducing a lateral drift towards and over the ADCP for bubbles to intersect the ADCP beams and cause data blanking. Above the data blanking (bubble) zones, V_{up} should decrease with height due to both buoyancy loss from bubble dissolution and small bubble detrainment (Leifer et al., 2015; Wilson et al., 2015).

2.5. CTD monitoring

The CTD used on both landers was a Seabird SBE-16Plus-V2 recording water conductivity, temperature, and pressure measurements once every 5 min located 0.20 m above the seafloor (http://www.seabird.com, 01/15/2015). The pressure sensor was a 7000 m digital-quartz sensor with ±1.4 m accuracy, resolution of less than 0.01 m, and was located 0.45 m lower than the hydrophone. Typical temporal signals in the CTD data are daily pressure fluctuations from ocean tides and seasonal temperature changes.

3. Results

The acoustic recordings from the two deployments at site 22/4b show a wide range of sounds, from anthropogenic events such as airguns from seismic exploration (Supplemental Fig. S1) and passing ships to natural sounds such as marine mammals (Supplemental Figs. S7 and S8), wind, and seafloor seep sounds. Below, we focus on seep-related sounds and ADCP-derived fluid velocities. A more detailed evaluation of the other recorded sounds is presented in the Supplemental Material.

3.1. Monthly average spectra

Sound pressure spectral levels averaged for each month were computed using the LTSAs and correcting for the calibrated hydrophone sensitivity (Fig. 5). Spectral levels generally decrease with frequency from 100 Hz to 10 kHz, with spectral peaks above 1000 Hz and slight overall level increases from summer to winter. Spectral levels between June and November varied less than a few dB re 1 μPa^2/Hz until a major event in December (see section 3.3 below). Significantly, recorded summer and fall spectral levels were 10–20 dB higher across the 100 Hz to 10 kHz band compared to many other oceanic sites (e.g., McDonald et al., 2006, 2008; McKenna et al., 2012; Roth et al., 2012). At low frequencies (up to ~500 Hz) seismic exploration air guns and ships, when present, were the dominant sources.

Above 500 Hz, spectral levels were elevated with spectral peaks that likely are associated with the seafloor seep system based on the long-term persistent character of the spectra and the absence of any other known sources. Before December, low frequency peaks occurred near 1.0, 1.5, and 2.5 kHz and are broad and poorly defined (Fig. 5). Using the Minnaert (1933) equation (1) for these band peaks and 120 m seabed crater depth, bubble radii would be ~4–10 mm, which are much larger than those observed at minor seeps (Leifer, 2010). Prior to October, the higher frequency peaks at 3.1, 3.6, and 5.1 kHz have a narrower bandwidth compared to the lower frequency peaks, and correspond to bubble radii of 3.5 to 2.1 mm, respectively, at 120 m depth, which still are larger than those reported for shallower, smaller seeps offshore of southern California (Leifer and Tang, 2007). In December and January, the main, low-frequency spectral peak was elevated by about 10–15 dB, with the peak shifted downward in frequency and broadened in bandwidth; whereas, many of the spectral peaks above 2 kHz increased in strength while maintaining the same frequency but are less well-defined and appear to be somewhat masked over the frequency band (Fig. 5).

It was not known *a priori* how far away various active vents were from the hydrophone during the recordings and because a hydrophone array was not deployed, direct application of the methods from Leighton and White (2012) cannot be used to estimate vent fluxes. Still, a comparison of the observed spectral levels for the 22/4b site (Fig. 5) with spectral source levels from Leighton and White (2012) is useful in a qualitative manner. For example, Figure 1 from Leighton and White (2012) shows the theoretical

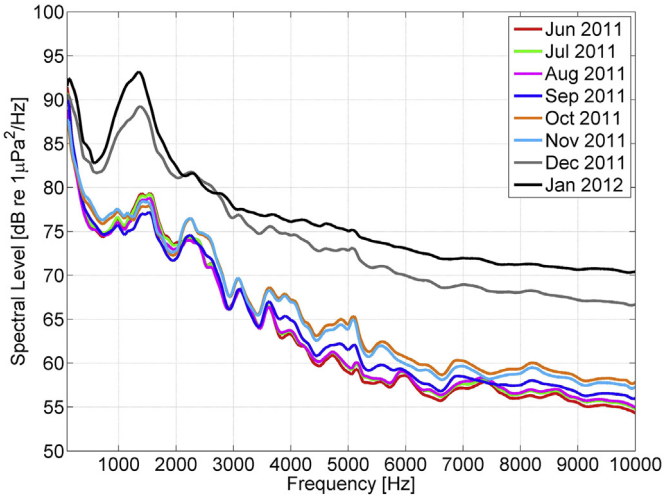

Figure 5. Monthly average sound pressure spectral levels from hydrophone-calibrated, decimated, Long-Term Spectral Average (LTSA) in units of sound pressure spectral density and 1 Hz bandwidth from 0.1 to 10 kHz.

forward model source level spectra based on Leifer and Culling's (2010) minor seep (0.57 cm^3 s^{-1}) which is similar to the peaky spectra prior to December (Fig. 5). Although, the spectra for the theoretical minor seep was corrected for range relative to 1 m, its peak levels were about 8 dB lower than June and July for this site (uncorrected for range), suggesting higher flow or multiple vents with similar size bubbles near the hydrophone. Figure 3 from Leighton and White (2012) shows the theoretical forward model source level spectra based on Leifer and Culling's (2010) major seep (10.4 cm^3 s^{-1}) which has the elevated and smoother spectral characteristics from December and January at site 22/4b (Fig. 5). Again, 22/4b spectral levels are about 7–8 dB higher than for the theoretical source spectra suggesting higher flow because it is unlikely the source was less than 1 m from the hydrophone based on visual observations of the nearby seafloor during Lander deployment and recovery. However, given that five major seabed plumes were located within 20 m of the hydrophone and were directly quantified at 0.5–3 L s^{-1} (Leifer, 2015), a factor of 50–300 higher than the major seep in Leifer and Culling (2010), and given that the total crater seabed flux was estimated at 90 L s^{-1} (Leifer, 2015), higher received levels were expected. The lower than expected levels may be a result of acoustic propagation loss created by signal scattering and interference from the many bubble plumes.

3.2. Long-term spectral averages and acoustic anomalies

LTSAs and daily-mean acoustic anomalies show a pattern of increased and decreased activity over various time scales for the two recording periods (Fig. 6). In the first deployment (June–September; Fig. 6a), there was a slight downward trend in acoustic energy followed in the second deployment (September–January; Fig. 6b) by a larger upward trend until a major event on 8 December raised levels by more than 10 dB. After this event, the average acoustic energy decreased until the end of the recording. Events lasting a few days, such as the peaks around 24 July and 28 August, often were related to nearby storm wind events; whereas, the single day events on 10 and 18 September were from the support ship while it was near the deployment site. Semi-diurnal events during July and early August appear as vertical striations in the LTSA and are correlated with local tides such that acoustic level highs occur when the sea level is high (see Supplemental material, Figs. S2–S4). As this pattern weakens, a strong diurnal pattern is apparent and continues into November. Also, an increase in levels for the band around ~2.2 kHz are observed in the second deployment (late September through early December; Fig. 6b), which was far more prominent than in the late summer in the first deployment. Also observed during the fall are increases in the monthly average spectral level in the frequency band peaks above ~2 kHz (Fig. 5).

3.3. Acoustic event 8 December 2011

During the second deployment, a major transient acoustic event was detected on 8 December 2011 around 20:20:20 GMT, interpreted as an eruption. A high temporal and spectral resolution spectrogram and acoustic anomalies for the frequency bands 1–3 kHz and 0.03–100 kHz during the event provide a detailed time sequence (Fig. 7). The event appears to have a discrete initiation (~20:20:16) with spectral levels increased across the full frequency band after the event begins.

Before the eruption, the acoustic energy was quasi steady-state across the two bands plotted in Figure 7, with near zero acoustic anomalies. An initial pulse at ~20:20:16 signaled the beginning of the event, with acoustic energy spreading to 100 kHz, the Nyquist frequency, and thus likely higher. The eruption built up over the next few seconds cresting ~4 s after the initial pulse at ~20:20:20. After a few more seconds, the acoustic energy decreased rapidly to pre-eruption levels and remained at those levels for about 1 s before another short-lived eruption of similar strength to the initial burst occurred (20:20:24), which only lasted ~1 s. Although energy in the 1–3 kHz band remained constant for the next 3 s, across the broader frequency range, it remained slightly elevated with occasional pulses. At ~12 s after the initial pulse (~20:20:28), energy in the 1–3 kHz band decreased by almost 20 dB below pre-eruption levels, while the energy at higher frequencies was steady or slightly increasing.

After the event (~20:20:40), the broad-band sound levels return to quasi steady-state but at far higher levels than before the event, including new emissions at frequencies well above 3 kHz. Although an increase in acoustic strength can arise from an increase in emissions or a decrease in spatial distance, the appearance of emission at higher frequencies signifies a real change in seepage and almost certainly is related to activation of more energetic vents or transformation of lower energy vents to higher emission vents, such as would have been created by the eruption. Higher emission vents produce bubbles spanning a wider size range, including smaller bubbles that require more energy to form (Leifer, 2010), and thus would produce higher frequency components.

3.4. ADCP long-term and event 8 December 2011

Strong upward vertical fluid velocities are proportional to the integrated emission of the bubble plume (Leifer et al., 2009), and thus changes in emission manifest as changes in the upwelling flow. Coincident with the acoustic event observed on 8 December there was a dramatic increase in the upwelling flow, and also evidence that the upwelling flow began to penetrate to almost the sea surface (Fig. 8). Data blanking indicates where bubbles drifted into the ADCP data, a phenomenon that also became far more extensive after the 8 December event, when values of V_{up} to 1.5 m s^{-1} were observed.

In fall 2011, during the second deployment, there was a significant increase in V_{up} and less data blanking in the upper water column than during the first deployment in the summer 2011 (Fig. 8). These changes most likely arose because the two landers were at slightly different locations and orientations relative to the seep bubble plumes (Nauw et al., 2015).

Monthly-averaged upwelling velocity probabilities, P_{Vup}, were calculated to identify seepage-driven changes with time (Fig. 9) and showed the strongest V_{up} was between depths of 15 and 70 m; whereas, the minimum V_{up} was at 30–35 m (i.e., the thermocline). Changes in the upwelling probability distribution are indicators of changes in the seepage emission spatial distribution and strength. P_{Vup} was calculated with no overlap and data blanked samples and outliers were not included in the P_{Vup} calculation.

Monthly P_{Vup} show patterns in each season and significant differences before and after the 8 December event. Summer P_{Vup} was dominated by a weak upwelling flow throughout most of the deeper water column (Fig. 9, feature a), and a secondary stronger V_{up} "branch" beginning in the lower water-column (Fig. 9, feature b). This secondary branch rapidly accelerates through the water column, before leaving the ADCP beams at ~60 m. This branch pattern, does not match with the strong upper water column (<30 m) pattern (Fig. 9, feature c) where the main plume had drifted over the ADCP (as indicated by blanking – Fig. 8). These patterns are consistent with the ADCP mapping momentum flows for two distinct plumes, and is consistent with sonar data showing two or three dominant plumes comprising the megaplume (Schneider von Deimling et al., 2015; Wilson et al., 2015).

Through November, the weak upwelling "core" decreased continuously in probability (Fig. 9, feature a), while upper water-

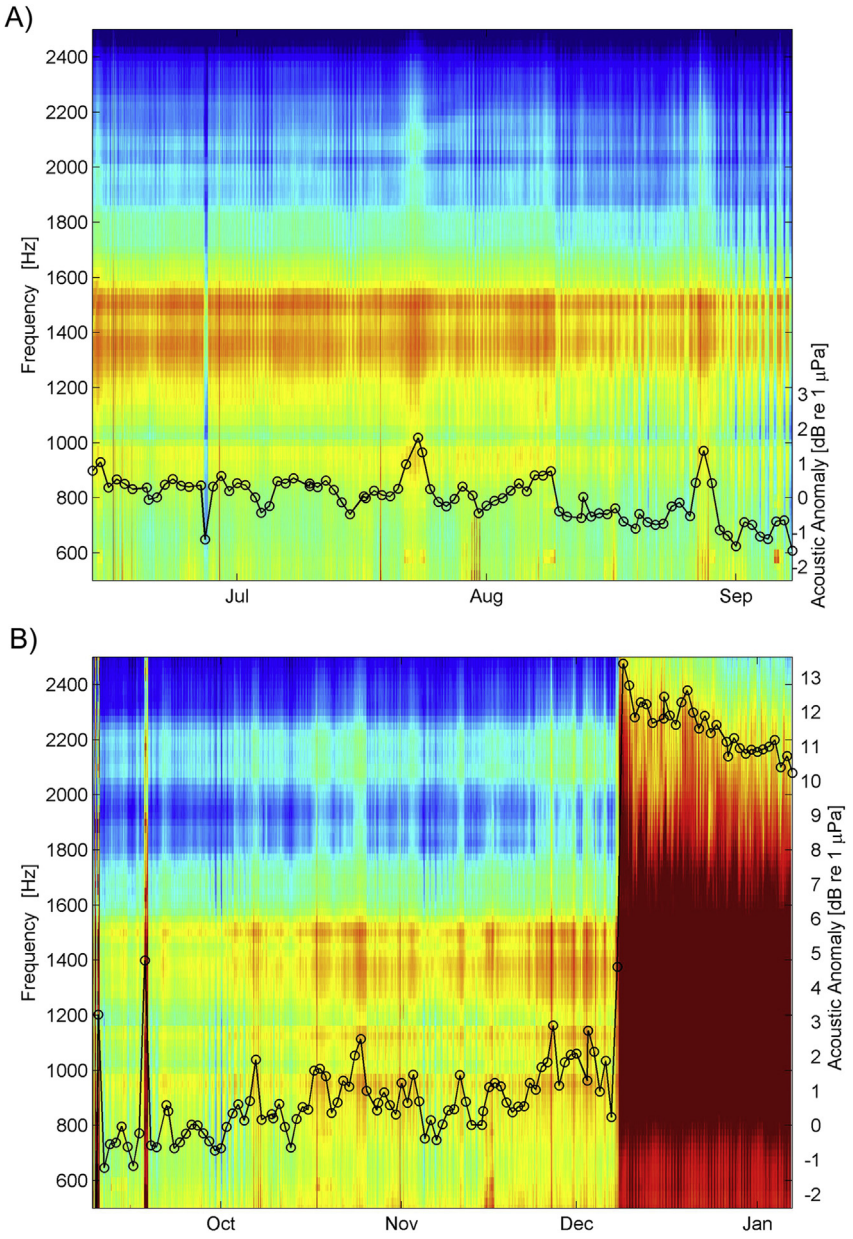

Figure 6. Long-Term Spectral Average (LTSA) with daily mean acoustic anomaly. LTSA warm colors represent higher intensity sound than cool colors and 5 s spectral averages were averaged again to 1 h with 25 Hz frequency bins. Acoustic anomalies (black circles) are averaged from 1 to 3 kHz over 1d with axis on right. A) First deployment (88 d) shows a slight downward trend in acoustic anomaly. Peaks near 24 July and 29 August are from nearby storms. B) Second deployment (121 d) shows a general upward trend precedes the major eruptive event on 8 December, after which there is a downward trend in the acoustic anomaly. Large, single day peaks at 10 and 18 September are from the deployment ship, *S/V Noordhoek Pathfinder*, while near site 22/4b. (For interpretation of the references to color in this figure legend, the reader is referred to the web version of this article.)

column upwelling strengthened near the sea surface. The early summer branch (Fig. 9, feature b) was joined in August by a secondary branch (Fig. 9, feature d), with both branches increasing in probability. By November, the central weak feature (Fig. 9, feature a) had weakened to the point of almost disappearing. This trend suggests the site shifted from emissions dominated by a single plume to one dominated by many plumes.

Peak V_{up} was around the thermocline (Fig. 9, feature c) from summer to November. However, starting in December, the strongest V_{up} was ~10 m below the sea surface (Fig. 9, feature e). In addition, a strong upwelling flow continued at the thermocline (Fig. 9, feature f); and at a significantly higher V_{up} than in autumn and summer. This thermocline core decreased in strength over the winter into the late spring (Fig. 9, feature f). A significant weakening in V_{up} also appeared in March 2012 with the reappearance of very slight upwelling flows in the bottom 20 m of the water column (Fig. 9, feature g), increasing in probability into April.

A significant change also occurred from near the sea surface. Through the summer until November, near sea surface velocities were zero or close to zero. However, beginning in December, strong V_{up} persisted to at least a few meters from the sea surface (the ADCP does not acquire data to the sea surface, particularly in the presence of strong waves). The penetration of upwelling flows almost to the sea surface demonstrates that significant bubbles were reaching the sea surface. Prior to the 8 December event, upwelling flows did not reach the sea surface, although due to plume advection by tides, which follow a directional ellipse, such flows would

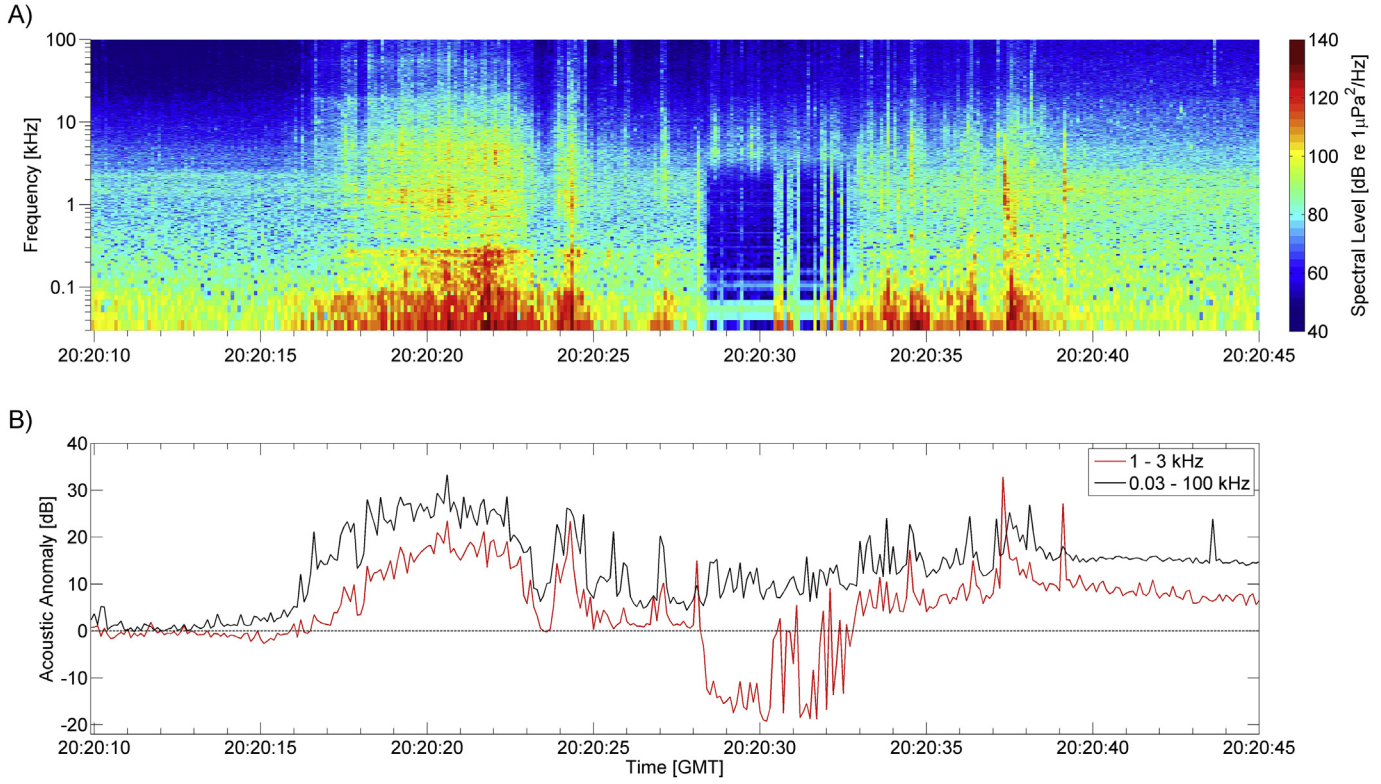

Figure 7. A) High resolution (0.1 s and 10 Hz) spectrogram with base-10 logarithmic frequency axis, corrected for hydrophone transfer function, and B) acoustic anomalies for 1–3 kHz (red) and 30 Hz–100 kHz (black) bands from just before to just after 8 December 2011 eruptive event. 0 dB is energy before the eruption. The spectrogram was calculated with non-overlapping 0.1 s Hanning windows (10 Hz resolution) and was plotted from 30 Hz to 100 kHz. Acoustic anomalies were calculated using Equation (2) except the sound pressure spectral level matrix, S_{ij}, was the high resolution spectrogram and the average spectra, $\bar{S}_i$, was calculated from an earlier period at 20:19:00. High frequency, narrow pulses at 20:25.5 and 20:43.5 are pings from the ADCP. (For interpretation of the references to color in this figure legend, the reader is referred to the web version of this article.)

have passed through the beam at some point during the tidal cycle. Furthermore, the absence of a strong upwelling flow was consistent with visual observations at the sea surface during the September field trip (Leifer and Judd, 2015; Nauw et al., 2015).

The event on 8 December corresponded closely in time with significantly higher V_{up} (Fig. 10A), which also correlated with greater data blanking. Data blanking requires current advection of the bubble plume into the ADCP beam, and thus was modulated by the tidal cycle. Data blanking events occurred consistently with a loose correlation between the highest upwelling flow; however, they did not immediately occur strongly right after the eruptive event, blanking only a few meters near the seabed. Upwelling flows were stronger at 12:00 9 December, as was data blanking extent, but less than subsequent data blanking events that extended to ~80 m depth. The data blanking on 15:00 10 December lasted far longer (~6 h) and started deeper (~109 m) than the earlier data blanking events after the blowout. The significant increase in depth of the data blanking implies the source was closer, which also was consistent with the longer blanking (bubbles in the ADCP beams over a larger portion of the tidal cycle and hence direction). The latter two noted blanking events corresponded to horizontal flows with a strong north current, while the first two after the 8 December event corresponded to stronger horizontal east currents (Fig. 10A). Thus, the upwelling flow corresponds to different sources. Data blanking was a persistent feature through March 2012.

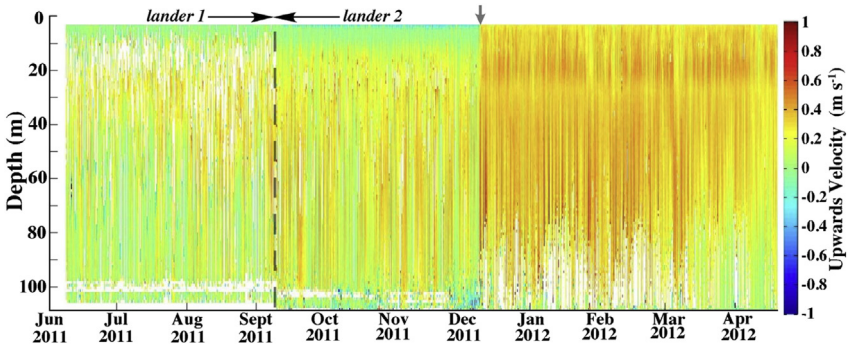

Figure 8. Upwelling velocity from ADCP data for both deployments. Velocities restricted to the range −1 to 1 m s^{-1} with scale on right. White regions are data blanked from bubble contamination. Downward arrow indicates 8 December 2011 event, and dotted line delineates the two lander deployments.

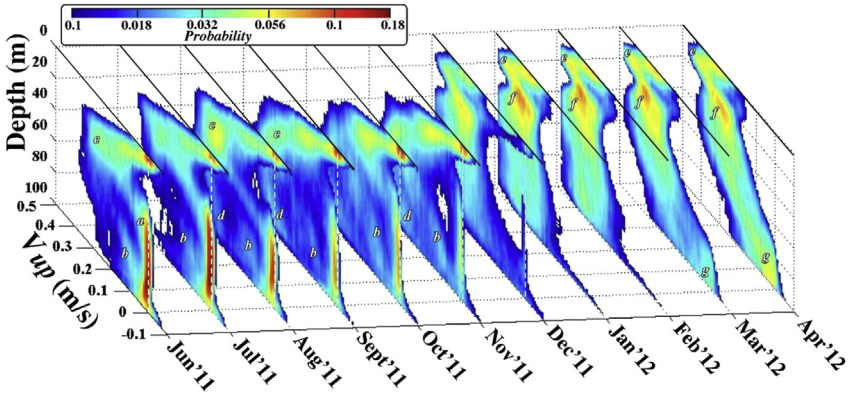

Figure 9. Monthly upwelling velocity, V_{up}, probability distributions, P_{Vup}. Key features labeled *a–g* and are described in section 3.4 of this manuscript.

3.5. CTD and ROV observations

The CTDs provided a record of pressure (i.e., depth) over the deployments showing a rising and falling pattern correlated with the changing tides. The 8 December event clearly was recorded by the CTD as a large depth increase (~6 m) of the Benthic Lander (Fig. 10B). Close inspection of the event showed that the lander depth lifted by ~1 m for several hours before the abrupt ~6 m drop at 20:20, followed by an additional elevation drop of almost 1 m in the following few hours to a final depth of 118.5 m. Additionally, the CTDs' salinity recordings (not shown) indicated a decrease to less than 31.5 parts per thousand (ppt) lasting ~14 h

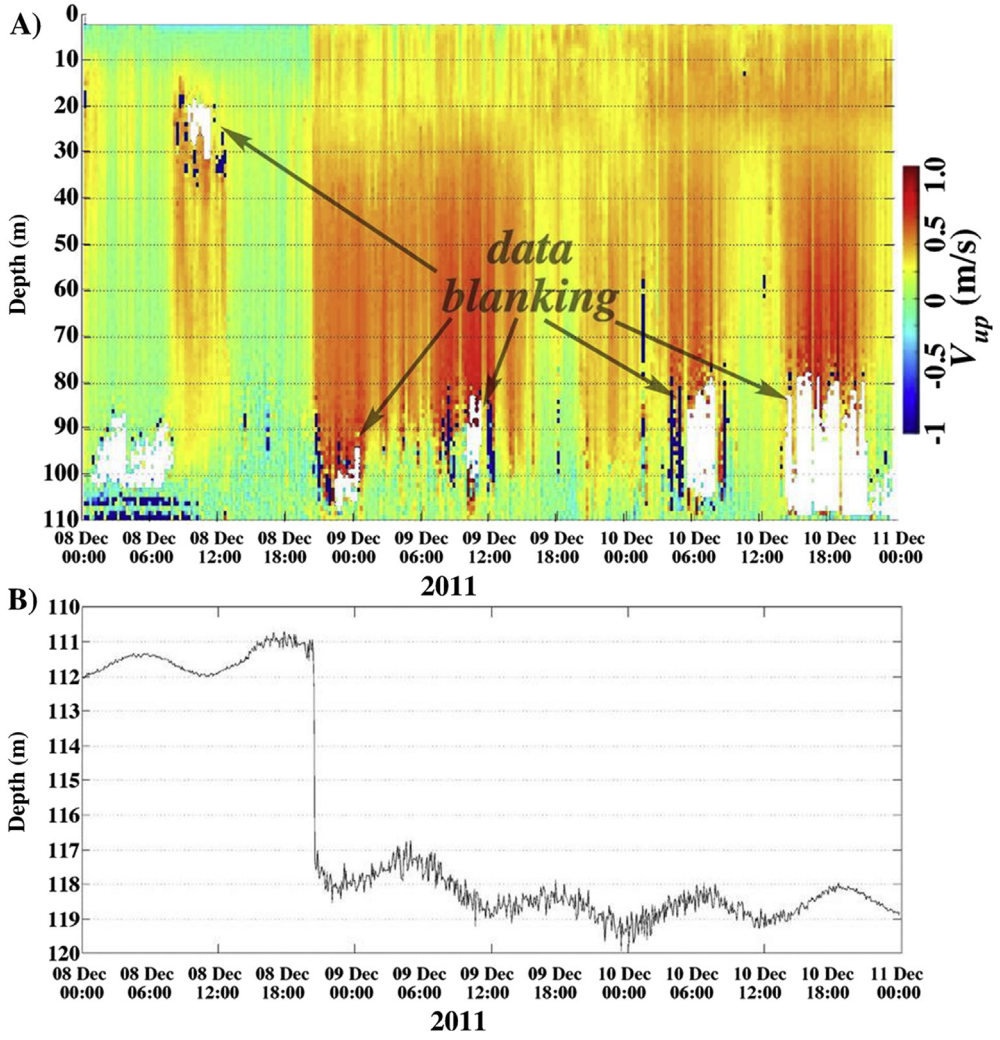

Figure 10. A) Vertical velocity profiles 8 to 11 December 2011 including event associated with the 8 December 2011 event. Velocity scale on right. Velocities clamped to color bar limits. B) CTD depth over same time period also shows 8 December 2011 event as an increase of ~6 m in depth. (For interpretation of the references to color in this figure legend, the reader is referred to the web version of this article.)

following the change in lander depth after which it rebounded to 33 ppt for nearly 2 weeks before returning to pre-event levels ~34 ppt.

Also consistent with interpretation of the 8 December event as an eruptive event were seabed crater morphology changes observed by an ROV in autumn 2012 (Linke, 2012), which documented a new jagged rift in the crater wall (Fig. 3). There were no such sharp crater wall features observed in fall 2011 during the video survey (Leifer, 2015; Schneider von Deimling et al., 2015). The new rift was ~1 m deep, ~2 m long, and contained a very strong bubble plume, far stronger than any individual major vent plumes observed in 2011 (Fig. 3).

4. Discussion

4.1. Long-term passive acoustic seep emission monitoring

Marine hydrocarbon seepage varies on a wide range of time scales from sub-second to decadal, thus absent long-term monitoring, extension of short-term flux measurements to longer time scales can be highly problematic. As a result, temporal variability often introduces far greater uncertainty in terms of characterizing site emissions than individual measurements, as observed for direct quantification of major plumes at 22/4b (Leifer, 2015). Additional uncertainty arises from spatial variability where emissions shift between and among vents (Leifer and Boles, 2005b; Greinert, 2008). Passive acoustic monitoring records the bubble formation sound (Minnaert, 1933) allowing long-term emission monitoring, and has been field demonstrated as quantitative for flux observations of minor bubble plumes, including bubble size distributions (Leifer and Tang, 2007). For both minor and major bubble plumes, spectrum levels can be used via an inverse process to estimate bubble size distributions and ultimately seep flux as long as the range from source to receiver is known (Leighton and White, 2012); although, greater uncertainty likely is introduced in seepage areas comprising numerous plumes with distinct bubble size distributions, and possible interferences between seep bubble plume acoustics.

The first step in effective use of PAM for seep monitoring is filtering-out from the recordings sounds unrelated to seepage. These include transient and short-term anthropogenic sources like airguns and ship propulsion and biotic sources like dolphins and porpoises, as well as longer duration natural sounds, such as storms and breaking waves. For example, strong wind events at a site several 100 km distant from 22/4b sometimes were correlated with increased acoustic anomalies, but not always. Examples of all these non-seep-related sounds were in the acoustic recordings and are shown in the Supplemental material.

In this study, PAM has been demonstrated as effective for long-term monitoring of seep emissions and identifying factors that control variability, such as tides and waves, particularly as part of the Benthic Lander. For low flow, minor vents, bubble frequency relates to size, and the formation rate allows derivation of quantitative flux values (Leifer and Tang, 2007). For low and high flow vents, the relationship between acoustic energy and emissions can be estimated if the range between the source and receiver is known, which could be accomplished in future studies with an array of appropriately spaced hydrophones (Leighton and White, 2012). However, in this study only a single omnidirectional hydrophone was used and acoustic energy changes only could be qualitatively analyzed in terms of emission changes. For example, monthly average sound pressure spectra showed that levels and spectral structure remained relatively stable for many months, with variability in the sound pressure identified as relating to tidal cycles.

The acoustic anomaly was correlated positively with tide height on a bi-weekly time scale and elevated acoustic levels occurred during periods of high sea level. Tidal variations have been observed in natural seepage in the Coal Oil Point (COP) seep field and were proposed as resulting from vent activation and deactivation in relationship to the changing hydrostatic pressure (Boles et al., 2001). Although tides also relate to currents, and cross flows influence emissions (Terasaka and Tsuge, 1993) a factor observed in the field (Leifer and Boles, 2005a), emissions from the bottom of the 22/4b crater are sheltered from the overlying ocean currents.

The generally low variability of the emissions is consistent with other observations (Boles et al., 2001) and with the resistance model of seepage (Leifer and Boles, 2005a; Leifer and Wilson, 2007). Specifically, the flux is driven by an overpressure above hydrostatic in the subsurface migration system, between a reservoir and the seabed. The flow pathways have a volume that provides a certain capacitance to the system. As a result, high flow systems must have low resistance to migration, with small external pressure changes having little effect on overall flow. In contrast, high resistance, low flow, low capacitance pathways can exhibit very large flow changes, up to activation and deactivation. In a sense, the system has a response time constant analogous to the electronic circuit equivalent of resistance and capacitance. On a finer scale, Leifer (2015) documented high temporal variability for individual vent plumes, including activation and deactivation. Thus, the mechanisms for changes in emission strength (i.e., activation and deactivation) are similar to those of Leifer and Boles (2005b); yet the response is opposite with respect to overpressure and tidal height.

Thus, the lack of high overall variability suggests that individual vent temporal variability may arise from emissions shifting between vents, with overall emissions far more constant than for any individual vent. Given the hundreds of individual vents – 176 vents observed and 440 estimated from the ROV video survey of the crater floor (Leifer, 2015) – contributing to the overall acoustic signature from 22/4b, the change in acoustic signal from spatial shifts likely also averages out with some vents shifting closer and some vents shifting farther. Furthermore, shifts between vents could result in shifts in bubble size distribution. The ROV video survey technicians reported apparent shifting between major vents (deactivation followed by nearby activation) which is consistent with a shell seabed and led to the hypothesis that the 22/4b seabed shares the characteristics of a trickle bed, allowing numerous fluid migration pathways (Leifer, 2015).

4.2. Acoustic monitoring of large transient events

Pockmarks are found widely on all coastal shelves and are manifest evidence of eruptive seepage related events (Judd and Hovland, 2009). Most aspects of their formation remain unclear, for example, it is unknown whether they are the result of single or multiple events, or from slow accretionary and erosional processes. Documentation of such elusive events requires either long-term monitoring or luck, and to some extent both.

During a brief scuba diver video survey at a megaplume in the COP seep field, Leifer et al. (2006) observed a sudden gas eruption after a short period when all emissions at the site ceased. The eruptive event lasted about 5 min. Fortuitous transport of the atmospheric methane plume to an onshore air monitoring station allowed estimation of emissions. Short-term monitoring of emissions with a turbine tent at the same megaplume seep area documented a far smaller eruptive event than a major vent, with peak emissions of 200 L s^{-1} (Leifer and Boles, 2005a). Again, prior to this eruption, which lasted ~5 s, emissions ceased. Emissions at a second turbine tent at the site did not decrease during this period. During the eruption, emissions gyrated wildly by a factor of four, while decreasing rapidly overall until emissions ceased. The

second no-flux period lasted only a short time, and then was followed by emissions rapidly increasing over 1 min in bursts before settling after a final burst that was approximately one-quarter of the emissions of the original burst. Then the system achieved a new, relatively steady-state emission that was more than double the pre-burst emission rate. Emissions then slowly decreased over the short dataset. Leifer and Boles (2005a) interpreted this as a blockage of a major migration pathway, followed by pressure buildup until the blockage suddenly cleared in the eruptive event. This event also depressurized the near seabed reservoir, leading to a cessation rather than diminution of emissions immediately post-eruption for the vents under the tent.

The COP seep field blowout characteristics in Leifer and Boles (2005a) show many similarities to the December 2011 acoustic recording for the 22/4b site. The eruption expanded the spectral range from the site by more than an order of magnitude, with strong levels up to 100 kHz, the recording system's limit. During the temporal Gaussian-shape eruption, which lasted about 5 s, acoustic energy varied dramatically on second and sub-second timescales, similar to the large emission variations observed by Leifer and Boles (2005a). These emission variations occurred over a wide spectral range. There was a short (~1 s) burst after a short (~1 s) near cessation of emissions and then about 3 s later the site emissions ceased across almost all frequencies for ~5 s. This would be consistent with depressurization of a shallow reservoir or dominant migration pathway ("main trunk") with connectivity to most vents in the crater. After the calm, for both the COP field eruption and the 22/4b eruption, emissions increased in a series of eruptive events of approximately similar strength. Finally, the 22/4b eruption stabilized after a final eruption at far higher acoustic levels that extended to far higher frequencies than before the event. This pattern is consistent with the observations by Leifer and Boles (2005a) who proposed that resistance in subsurface migration pathways after the eruptive event were reduced significantly, in part from the eruptive process, and that the reduction in resistance led to higher (measured) flow. Although a spatial shift could explain some or all of the increased acoustic levels, the presence of higher frequencies requires greater fluid dynamic energy to create the smaller-scale interfacial ruptures and formations associated with higher frequency sounds.

Further evidence that the acoustic changes corresponded to real emission changes was provided by the ADCP data, which showed an increase in upwelling flows after the acoustic eruption. Although the eruption resulted in the entire lander being repositioned to a deeper portion of the crater, the stronger upwelling flow also penetrated to nearly the sea surface. Because the plume shifts with the tidal ellipse, penetration to the sea surface, as opposed to largely dissipating 10–15 m below the sea surface, could not result from the lander repositioning. The sudden penetration of the upwelling flow to the sea surface in December indicates that far more bubbles were surviving to the sea surface than during the September expedition.

Overall, increased upwelling flow enhances bubble survival (Leifer et al., 2015) and allows smaller bubbles to reach the sea surface than for the weaker upwelling flows during the fall expedition, and before the eruptive event. However, to explain observations, Leifer et al. (2015) and Schneider von Deimling et al. (2015) hypothesized new mechanisms that would enhanced gas exchange rates in megaplumes, with the implication that solely increasing emissions leads to more rapid dissolution and is self-limiting. However, if as a result of the event, the bubble size distribution included far more large and very large bubbles, the driving buoyancy flux would persist to shallower depths. This would likely lead to greater direct methane transport to the atmosphere and also indirect methane transport to the sea surface by the upwelling flow of methane saturated waters.

This eruptive event likely destroyed in part or completely the ledge where the Lander was deployed and likely was related to the new sharp feature observed on the crater wall. The absence of any previous such sharp seabed crater features in fall 2011 deployment indicates that there must be erosive processes that slowly soften and eventually erase sharp features.

After the event, acoustic data were collected for an additional month during which acoustic energy slowly but significantly decreased. This appears superimposed on a longer time-scale trend of decreasing acoustic energy during the summer followed by slowly strengthening acoustic emissions during fall. The fall increase in acoustic emission corresponded to an increase in upwelling flow.

4.3. Long-term acoustic seep emission monitoring and seasonal oceanography

Distinct "seasonal" emissions characteristics were observed in the ADCP and seabed PAM recordings, which correspond loosely to important seasonal changes in the North Sea oceanography. Because the fluid and acoustic observations presented herein relate to seabed processes, the important North Sea oceanographic changes are those related to transfer of surface energy (winds and waves and storms) to the lower water column, a factor strongly controlled by the presence or absence of the thermocline. For much of the year, a strong thermocline is present from the late spring until mid-fall (Nauw et al., 2015), driven by the balance between tidal and wind-driven mixing and buoyancy generation by solar heating. Fronts that move slowly northwards develop at the transition between fully-mixed waters and stratified waters, typically passing 22/4b in November, after which the water column is fully mixed.

Although the North Sea is well known for storminess, the summer is relatively calm (Nauw et al., 2015). Beginning in autumn, storms begin to track frequently through the northern North Sea, continuing until spring and increasing in intensity during the winter months. Finally, in April/May, these storms decrease in intensity concomitant with the return of stratified conditions. Initially, autumn storms affect only the upper water column, with the thermocline shielding the seabed. But eventually, breakdown of the thermocline due to increasing storm intensity leads to a well-mixed water column and concomitant momentum and heat transfer across the water column. In 2011, the stormy season started with several short-lived, relatively weak storms in October, while November was relatively quiescent. Finally, in December the weather became dominated by very strong storms that continued until mid-late April. These summer, fall, and winter seasons were accompanied by an increase in the strength of horizontal currents, particularly the north–south component in the deeper water column, respectively (Nauw et al., 2015).

Winter upwelling flows penetrated all the way to the sea surface and exhibited a probability distribution distinctly different from those during summer and fall. In the summer, the flow pattern of weak upwelling to the thermocline is consistent with stratification presenting a significant barrier to the momentum plume. High velocities at the thermocline likely relate to instabilities in the interaction with the upwelling flow and the thermocline. In contrast, the lack of stratification is consistent with coherency of the momentum plume right to the sea surface. ADCP data showed indications of a reformation of the summer pattern near the seabed (Fig. 9, feature "g"), consistent with the storm data that showed the end of the winter storms in early April (Nauw et al., 2015).

Storms should affect and increase emissions, through hydrostatic pressure variations on the seabed, as well as the potential for storm currents to induce seabed scouring. Such behavior has been noted in the COP seep field where field-wide emissions increased during and immediately after storms (Leifer, unpublished

data). Overall acoustic energy (Fig. 5) showed three seasons in agreement with storms and ADCP current and upwelling data, a calm summer (Jun–Aug), a more active fall (Oct–Nov), and a far more active winter (Dec. and Jan.). Although some of the spectral differences could relate to greater seabed sound levels from moving sediments, the acoustic bubble emission modes (i.e., spectral peaks from 1 to 5 kHz and higher) all increased between the seasons suggesting stronger emissions. This in consistent with increased upwelling flow patterns for these three seasons, that suggests greater emissions in fall than summer. Given the significance of the 8 December event, overall winter acoustic emissions cannot be interpreted in a seasonal context; however, acoustic emissions increased during the last week of November and the first week of December (Fig. 6), when the first large storms arrived at the 22/4b site (Nauw et al., 2015).

5. Conclusion

Long-term acoustic monitoring of seafloor seeps in the North Sea shows variability on a wide range of time scales providing detailed information on seep activity including tidal influences and a major eruption on 8 December 2011. Spectral peaks from 1 kHz to >5 kHz persisted over much of the deployments, likely originating from multiple vents. The eruption, while lasting only a few seconds, was highly energetic and resulted in long-lasting elevated sound levels from 1 to 100 kHz, with the increased levels at high frequencies suggesting seep change associated with highly energetic vents. Post-eruption spectral levels in the 1–10 kHz band were elevated by ~10 dB.

Concurrent water column measurements of fluid velocity, pressure, and salinity also documented the 8 December eruption, but on a much coarser temporal scale than the PAM. ADCP upwelling velocities and bubble data blanking were increased post-eruption, supporting increased seep emission activity. Post–lander recovery ROV survey photos confirmed nearby major morphological changes in the crater wall along with strong bubble plumes consistent with an eruptive event.

This study showed that long-term PAM has great potential to improve our understanding of seep processes. However, there are significant areas needing further development. Specifically, investigative studies of the relationship between acoustic spectral energy and emission flux of bubble plumes, such as by Chen et al. (2012) in the laboratory and at natural marine seep sites as by Leifer and Tang (2007), need to be conducted for single and multiple plumes. Experiments with time-synchronized hydrophone arrays near vents for plume localization placed along with other flux measuring sensors could go a long way to improving PAM as a technique for estimating seep emission flux over long periods.

Acknowledgments

Our thanks go to the captain and crews of *S/V Noordhoek Pathfinder, R/Vs Alkor*, and *Heincke* for their excellent and professional work throughout the cruises where the Landers were deployed, exchanged and recovered. We thank Dr. Frank Wenzhöfer (MPI-Bremen, Germany) for the final recovery of the lander in April 2012. The technology and logistics center (TLZ) at GEOMAR is acknowledged for excellent logistic support, Matthias Türk is acknowledged for his help during Lander preparations. We thank Chris Garsha, Brent Hurley, Tim Christianson, John Hurwitz, Erin O'Neill, and Bruce Thayre from Scripps Whale Acoustic Laboratory for their engineering and technical support with HARP instrumentation and data processing operations. We thank Aaron Howard from Bubbleology Research International for providing wind data from the period of the first deployment. We thank two anonymous reviewers whose thoughtful and valuable comments greatly improved this manuscript. Thanks are given to the support of ExxonMobil under the direction of the UK Department of Environment and Climate Change (DECC), and to Simon Dewing, Joe Smith, and Gary Robertson (ExxonMobil) for help with this study. Views and opinions herein are solely those of the authors and do not imply endorsement by ExxonMobil or DECC.

Appendix A. Supplementary data

Supplementary data related to this article can be found at http://dx.doi.org/10.1016/j.marpetgeo.2015.02.011.

References

Asaeda, T., Imberger, J., 1993. Structure of bubble plumes in linearly stratified environments. J. Fluid Mech. 249, 35–57.
Baumann-Pickering, S., Wiggins, S.M., Roth, E.H., Roch, M.A., Schnitzler, H.-U., Hildebrand, J.A., 2010. Echolocation signals of a beaked whale at palmyra atoll. J. Acoust. Soc. Am. 127 (6), 3790–3799.
Boles, J.R., Clark, J.F., Leifer, I., Washburn, L., 2001. Temporal variation in natural methane seep rate due to tides, coal oil point area, California. J. Geophys. Res. – Oceans 106 (C11), 27,077–027,086.
Bradley, E.S., Leifer, I., Roberts, D.A., 2010. Long-term monitoring of a marine geologic hydrocarbon source by a coastal air pollution station in Southern California. Atmos. Environ. 44, 4973–4981.
Chen, L., Wood, S., Moore, S., Nguyen, B., 2012. Acoustic emission of bubbly flow and its size distribution spectrum. Proceedings of Acoustics 2012. Australian Acoustical Society, Fremantle, Australia, pp. 1–6.
Greinert, J., 2008. Monitoring temporal variability of bubble release at seeps: the hydroacoustic swath system GasQuant. J. Geophys. Res. 113, C07048.
IPCC, 2007. Climate Change 2007: Synthesis Report. Contribution of Working Groups I, II, and III to the Fourth Assessment Report of the Intergovernmental Panel on Climate Change. IPCC, Geneva, Switzerland, p. 104 P. Core Writing Team, R.K., and Reisinger, A.
Judd, A.G., Hovland, M., 2009. Seabed Fluid Flow: Impact of Geology, Biology and the Marine Environment. Cambridge University Press, p. 492.
Kvenvolden, K.A., Rogers, B.W., 2005. Gaia's breath-global methane exhalations. Mar. Petrol. Geol. 22 (4), 579–590.
Leifer, I., 2010. Characteristics and scaling of bubble plumes from marine hydrocarbon seepage in the coal oil point seep field. J. Geophys. Res. Oceans 115 (C11), C11014.
Leifer, I., 2015. Seabed bubble flux estimation by calibrated video survey for a large blowout seep in the North Sea. J. Mar. Petrol. Geol. (in this issue).
Leifer, I., Boles, J., 2005a. Measurement of marine hydrocarbon seep flow through fractured rock and unconsolidated sediment. Mar. Petrol. Geol. 22 (4), 551–568.
Leifer, I., Boles, J., 2005b. Turbine tent measurements of marine hydrocarbon seeps on subhourly timescales. J. Geophys. Research-Oceans 110 (C1).
Leifer, I., Boles, J.R., Luyendyk, B.P., Clark, J.F., 2004. Transient discharges from marine hydrocarbon seeps: spatial and temporal variability. Environ. Geol. 46 (8), 1038–1052.
Leifer, I., Culling, D., 2010. Formation of seep bubble plumes in the coal oil point seep field. Geo-Marine Lett. 30 (3/4), 339–353.
Leifer, I., Jeuthe, H., Gjøsund, S.H., Johansen, V., 2009. Engineered and natural Marine seep, bubble-driven buoyancy flows. J. Phys. Oceanogr. 39 (12), 3071–3090.
Leifer, I., Judd, A., 2015. The UK22/4b blowout 20 years on: Investigations of continuing methane emissions from sub-seabed to the atmosphere in a North Sea context. J. Mar. Petrol. Geol. (in this Issue).
Leifer, I., Kamerling, M., Luyendyk, B.P., Wilson, D., 2010. Geologic control of natural marine hydrocarbon seep emissions, coal oil point seep field, California. Geo-Marine Lett. 30 (3–4), 331–338.
Leifer, I., Luyendyk, B.P., Boles, J., Clark, J.F., 2006. Natural marine seepage blowout: contribution to atmospheric methane. Glob. Biogeochem. Cycles 20, GB3008.
Leifer, I., Solomon, E., Coffin, R., Rehder, G., Linke, P., 2015. The fate of bubbles in a large, intense bubble plume for stratified and unstratified water: numerical simulations of 22/4b expedition field data. J. Mar. Petrol. Geol. (in this Issue).
Leifer, I., Tang, D., 2007. The acoustic signature of marine seep bubbles. J. Acoust. Soc. Am. 121 (1), EL35–EL40.
Leifer, I., Wilson, K., 2007. The tidal influence on oil and gas emissions from an abandoned oil well: nearshore Summerland, California. Mar. Pollut. Bull. 54 (9), 1495–1506.
Leighton, T.G., White, P.R., 2012. Quantification of undersea gas leaks from carbon capture and storage facilities, from pipelines and from methane seeps, by their acoustic emissions. Proc. R. Soc. A: Math. Phys. Eng. Sci. 468 (2138), 485–510.
Linke, P., AL374 cruise participants, 2011. RV ALKOR Fahrtbericht/Cruise Report AL374; 29.05.-14.06.2011, Kiel - Kiel; ECO2-sub-seabed CO2 Storage: Impact on Marine Ecosystems. IFM-geomar Report. 51, IFM-GEOMAR, Kiel, p. 55. http://dx.doi.org/10.3289/IFM-GEOMAR_REP_3251_2011.
Linke, P. (Ed.), 2012. RV Celtic Explorer EUROFLEETS Cruise Report CE12010-eco2@northsea: 20.07. – 06.08.2012. GEOMAR, Kiel, Germany, p. 60. Bremerhaven - Hamburg. GEOMAR Report, N. Ser. 004 http://dx.doi.org/10.3289/GEOMAR_REP_NS_3284_2012

Mastepanov, M., Sigsgaard, C., Dlugokencky, E.J., Houweling, S., Strom, L., Tamstorf, M.P., Christensen, T.R., 2008. Large tundra methane burst during onset of freezing. NATURE 456 (7222), 628–630.
McDonald, M.A., Hildebrand, J.A., Wiggins, S.M., 2006. Increases in deep ocean ambient noise in the Northeast Pacific west of San Nicolas Island, California. J. Acoust. Soc. Am. 120 (2), 711–718.
McDonald, M.A., Hildebrand, J.A., Wiggins, S.M., Ross, D., 2008. A 50 Year comparison of ambient ocean noise near San Clemente Island: a bathymetrically complex coastal region off Southern California. J. Acoust. Soc. Am. 124 (4), 1985–1992.
McKenna, M.F., Ross, D., Wiggins, S.M., Hildebrand, J.A., 2012. Underwater radiated noise from modern commercial ships. J. Acoust. Soc. Am. 131 (1), 92–103.
Milgram, J.H., 1983. Mean flow in round bubble plumes. J. Fluid Mech. 133, 345–376.
Minnaert, M., 1933. On musical air bubbles and the sound of running water. Philos. Mag. 16, 235–248.
Nauw, J., Linke, P., Leifer, I., 2015. Bubble momentum plume as a mechanism for an early breakdown of the seasonal stratification in the northern North Sea. Mar. Petrol. Geol. (in this issue).
Oleson, E.M., Wiggins, S.M., Hildebrand, J.A., 2007. Temporal separation of blue whale call types on a southern California feeding ground. Anim. Behav. 74 (4), 881–894.
Peischl, J., Ryerson, T.B., Brioude, J., Aikin, K.C., Andrews, A.E., Atlas, E., Blake, D., Daube, B.C., de Gouw, J.A., Dlugokencky, E., Frost, G.J., Gentner, D.R., Gilman, J.B., Goldstein, A.H., Harley, R.A., Holloway, J.S., Kofler, J., Kuster, W.C., Lang, P.M., Novelli, P.C., Santoni, G.W., Trainer, M., Wofsy, S.C., Parrish, D.D., 2013. Quantifying sources of methane using light alkanes in the Los Angeles basin, California. J. Geophys. Res. Atmos. 118, 4974–4990.
Quigley, D.C., Hornafius, J.S., Luyendyk, B.P., Francis, R.D., Clark, J., Washburn, L., 1999. Decrease in natural marine hydrocarbon seepage near coal oil point, California, associated with offshore oil production. Geology 27 (11), 1047–1050.
Rehder, G., Keir, R., Suess, E., Pohlmann, T., 1998. The multiple sources and patterns of methane in North Sea waters. Aquatic Geochemistry 4 (3–4), 403–427.
Roth, E.H., Hildebrand, J.A., Wiggins, S.M., Ross, D., 2012. Underwater ambient noise on the chukchi Sea continental slope from 2006–2009. J. Acoust. Soc. Am. 131 (1), 104–110.
Sauter, E.J., Muyakshin, S.I., Charlou, J.-L., Schlüter, M., Boetius, A., Jerosch, K., Damm, E., Foucher, J.-P., Klages, M., 2006. Methane discharge from a deep-sea submarine mud volcano into the upper water column by gas hydrate-coated methane bubbles. Earth Planet. Sci. Lett. 243 (3–4), 354–365.
Schneider von Deimling, J., Brockhoff, J., Greinert, J., 2007. Flare imaging with multibeam systems: data processing for bubble detection at seeps. Geochem. Geophys. Geosyst. 8 (6). http://dx.doi.org/10.1029/2007gc001577.
Schneider von Deimling, J., Greinert, J., Chapman, N.R., Rabbel, W., Linke, P., 2010. Acoustic imaging of natural gas seepage in the North Sea: Sensing bubbles controlled by variable currents. Limnol. Oceanogr. Methods 8 (1960), 155–171.
Schneider von Deimling, J., Rehder, G., Linke, P., Judd, A., 2015. Rediscovery of an abandoned well in the North Sea: 22/4b site characterization since 2005 about a massive gas plume release into the water column. J. Mar. Petrol. Geol. (in this issue).
Shakhova, N., Semiletov Igor, P., Leifer, I., Sergienko, V., Salyuk, A., Kosmach, D., Chernikh, D., Stubbs, C., Nicolsky, D., Tumskoy, V., Alexeev, V., Gustafsson, O., 2013. Ebullition and storm-induced methane release from the East Siberian Arctic Shelf. Nat. Geosci. 7, 64–70.
Soldevilla, M.S., Henderson, E.E., Campbell, G.S., Wiggins, S.M., Hildebrand, J.A., Roch, M.A., 2008. Classification of Risso's and pacific white-sided dolphins using spectral properties of echolocation clicks. J. Acoust. Soc. Am. 124 (1), 609–624.
SonTek, 1990. Acoustic Doppler Profiler Principles of Operation. SonTek, San Deigo, CA, p. 28.
Terasaka, K., Tsuge, H., 1993. Bubble formation under constant-flow conditions. Chem. Eng. Sci. 48 (19), 3417–3422.
Vazquez, A., Sanchez, R.M., Salinas-Rodrigues, A., Soria, A., Manasseh, R., 2005. A look at three measurement techniques for bubble size distribution. Exp. Therm. Fluid Sci. 30, 49–57.
Washburn, L., Clark, J.F., Kyriakidis, P., 2005. The spatial scales, distribution, and intensity of natural marine hydrocarbon seeps near coal oil point, California. Mar. Petrol. Geol. 22 (4), 569–578.
Welch, P.D., 1967. The use of fast fourier transform for the estimation of power spectra: a method based on time averaging over short, modified periodograms. IEEE Trans. Audio Electroacoustics AU-15 70–73.
Wiggins, S.M., 2003. Autonomous acoustic recording packages (ARPs) for long-term monitoring of whale sounds. MTS J. 37 (2), 13–22.
Wiggins, S.M., Frasier, K.E., Elizabeth Henderson, E., Hildebrand, J.A., 2013. Tracking dolphin whistles using an autonomous acoustic recorder array. J. Acoust. Soc. Am. 133 (6), 3813–3818.
Wiggins, S.M., Hildebrand, J.A., 2007. High-frequency acoustic recording package (HARP) for broad-band, long-term marine mammal monitoring. International Symposium on Underwater Technology 2007 and International Workshop on Scientific Use of Submarine Cables & Related Technologies 2007, (IEEE, Tokyo, Japan), pp. 551–557.
Wilson, D., Leifer, I., Maillard, E., 2015. Megaplume bubble process visualization by 3D multibeam sonar mapping. J. Mar. Petrol. Geol. (in this issue).
Wüest, A., Brooks, N.H., Imboden, D.M., 1992. Bubble plume modeling for lake restoration. Water Resour. Res. 28 (12), 3235–3250.
Zimmer, W., 2011. Passive acoustic monitoring of cetaceans. Cambridge University Press, Cambridge, p. 356.